Nano Research

Open Access

Research Article

A $CuCrP_2S_6$-based lateral memristor for in-materia reservoir computing in temporal information processing

Yongqing Huang[1,2,3,§], Runhua Zhang[3,5,§], Jiaxiang Chen[3,4], Liuqi Cheng[3,4], Zhihao Li[3,4], Chao Hu[3], Jiahong Yang[3], Ning Li[2], Binbin Zhang[2], Qi Dai[2], Xiangcheng Li[1], Zhenrong Zhang[1] ✉, Qijun Sun[3,4] ✉, Jinran Yu[2] ✉, and Chaofan Zhang[2] ✉

[1] Guangxi Key Laboratory of Multimedia Communications and Network Technology, School of Computer, Electronics and Information, Guangxi University, Nanning 530004, China
[2] College of Advanced Interdisciplinary Studies & Nanhu Laser Laboratory, National University of Defense Technology, Changsha 410073, China
[3] Beijing Institute of Nanoenergy and Nanosystems, Chinese Academy of Sciences, Beijing 101400, China
[4] School of Nanoscience and Engineering, University of Chinese Academy of Sciences, Beijing 100049, China
[5] School of Science, China University of Geosciences, Beijing 100083, China
[§] Yongqing Huang and Runhua Zhang contributed equally to this work.

Cite this article: *Nano Research*, **2026**, *19*, 94908805. https://doi.org/10.26599/NR.2026.94908805

ABSTRACT: Silicon-based accelerators deliver high computational precision through the von Neumann architecture, yet incur substantial energy costs due to frequent data movement and discrete logic switching. In contrast, in-materia reservoir computing harnesses the intrinsic nonlinear dynamics of materials to enable energy-efficient temporal information processing, offering a promising route toward neuromorphic hardware. Here, we report a two-terminal lateral memristor based on two-dimensional (2D) ferroelectric $CuCrP_2S_6$, where electric-field-driven Cu^+ ion migration yields continuously tunable nonlinear conductance, short-term memory, and rich relaxation dynamics—properties that closely match the physical requirements of reservoir computing. On this basis, pattern recognition and chaotic prediction were implemented. On the Modified National Institute of Standards and Technology (MNIST) database handwritten digit benchmark, the system achieves 88.91% accuracy. Furthermore, the reservoir achieved normalized root-mean-square errors (NRMSE) of 0.02732 and 0.3716 for autonomous prediction of the Hénon map (steps 500–550) and the Mackey-Glass (steps 500–600) time series, respectively. These results establish $CuCrP_2S_6$ lateral memristors as an in-materia reservoir platform for temporal information processing and highlight their potential for advancing post-Moore neuromorphic computing systems.

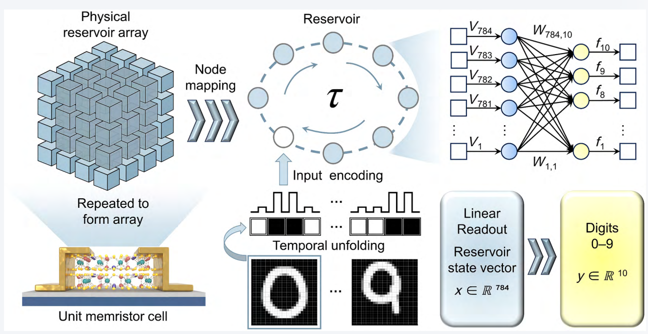

KEYWORDS: $CuCrP_2S_6$ lateral memristor, Cu^+ ion migration, in-materia computing, reservoir computing, temporal information processing

1 Introduction

As data-intensive workloads continue to scale, the dominant cost of computation increasingly shifts from arithmetic operations to data movement, amplifying demand for energy-efficient neuromorphic accelerators. Reservoir computing (RC)—a recurrent framework that trains only the readout layer—has emerged as a low-complexity solution for temporal tasks [1–4]. Its core principle leverages a fixed nonlinear reservoir to project inputs into high-dimensional space, enabling efficient readout training via linear regression [5]. Time multiplexing with virtual nodes can expand the effective reservoir dimension and improve the representation of temporal dynamics [6, 7].

Conventional RC implementations face energy inefficiency and limited nonlinearity in software or CMOS-based hardware [8, 9], driving exploration of in-materia RC platforms leveraging intrinsic

Received: March 19, 2026; **Revised:** April 14, 2026
Accepted: May 3, 2026

✉Address correspondence to Chaofan Zhang, c.zhang@nudt.edu.cn; Jinran Yu, yujinran@ucas.ac.cn; Qijun Sun, sunqijun@binn.cas.cn; Zhenrong Zhang, zzr76@gxu.edu.cn

material dynamics [10–13]. Two-dimensional van der Waals (vdW) materials emerge as particularly compelling candidates, owing to their atomic thickness, high-quality interfaces, and strong electron-ion coupling [14, 15]. In addition, vdW layered materials further provide well-defined ion migration pathways and tunable defect landscapes, enabling efficient and controllable ionic transport [16, 17]. Critically, layered chalcogenides (e.g., $CuInP_2S_6$, $CuCrP_2S_6$ (CCPS)) exhibit reversible field-driven metal-ion (Cu^+) migration, yielding nonlinear conductance tuning and synapse-like plasticity behaviors including long-term potentiation/depression (LTP/LTD) [18, 19]. These properties make them promising candidates for time-dependent hardware reservoirs and neuromorphic computing. In addition, recent memristor-network-based neuromorphic systems have demonstrated ultralow-power and reconfigurable information processing, further highlighting the promise of memristive hardware for intelligent computing [20, 21]. Wu et al. demonstrated Cu^+ ion-migration-driven dynamics in $CuInP_2S_6$ memristors for benchmark time-series prediction and temperature forecasting [16]. Wang et al. achieved 90.43% MNIST accuracy via optoelectronic synapses based on $CuInP_2S_6/MoS_2$/graphene [22]. Cheng et al. reported $CuCrP_2S_6$-based memristive synapses achieving 98.85% accuracy on MNIST and 96.4% accuracy in spoken-digit recognition [18]. Together, these studies highlight the promise of Cu-based van der Waals ionic conductors for neuromorphic and reservoir-computing hardware. Representative memristor-based reservoir systems have demonstrated the feasibility of temporal information processing, motivating further exploration of van der Waals ionic materials for physically implemented reservoirs.

In this work, we demonstrate a two-dimensional ferroelectric CCPS lateral memristor as a physically interpretable in-materia reservoir, where reversible Cu^+ ion migration directly gives rise to the nonlinear and fading memory dynamics required for temporal information processing. Figure 1(a) schematically depicts the device structure and its scalable physical reservoir array architecture via unit cell replication. Precise control of ionic kinetics is achieved through bias amplitude and sweep rate tuning, yielding programmable synaptic plasticity with pA-level read currents. Time-dependent conductance relaxation reveals pronounced short-term memory (STM) effects that naturally fulfill the core requirements of RC, including nonlinearity and fading memory. These characteristics establish CCPS-based lateral memristors as a robust physical platform for time-multiplexed reservoir computing networks.

2 Results and discussion

2.1 Material characterization and field-driven ionic conduction

Figure 1(b) shows a representative CCPS lateral memristor fabricated by mechanical exfoliation of bulk crystal and PDMS-assisted transfer onto SiO_2/Si (285 nm SiO_2), with Cr/Au electrodes (10/50 nm) patterned via electron-beam lithography and thermal evaporation. CCPS is a vdW layered material in which metal cations are confined in sulfur-coordinated octahedral frameworks, while adjacent layers are coupled through weak vdW interactions [18, 23, 24]. The weak bonding between Cu^+ and $(P_2S_6)^{4-}$ units enables intrinsic ionic mobility, establishing the foundation for field-driven conductance modulation [25]. Energy-dispersive X-ray spectroscopy (EDS) mapping (Fig. 1(c)) reveals uniform distribution of Cu, Cr, P, and S across the nanoflake, corroborated by the stoichiometric Cu:Cr:P:S ratio of 1:1:2:6 derived from the EDS spectrum (Fig. 1(d)) [25]. Atomic force microscopy (AFM) analysis of the fabricated device reveals a uniform CCPS flake thickness of ~ 75 nm (Fig. S1 in the Electronic Supplementary

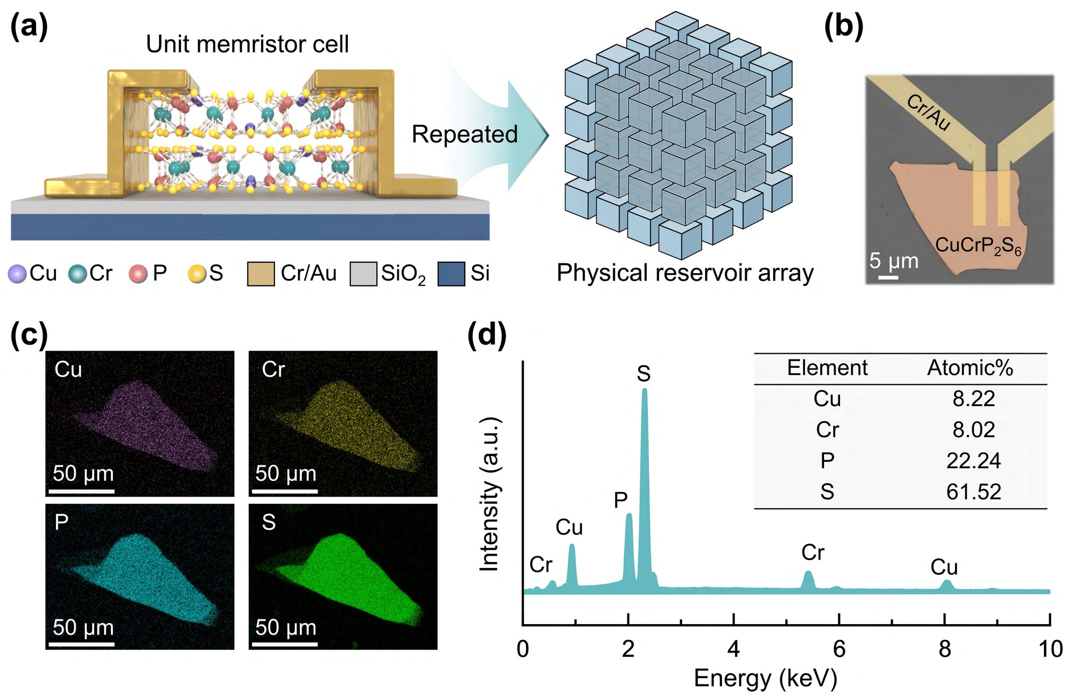

Element	Atomic%
Cu	8.22
Cr	8.02
P	22.24
S	61.52

Figure 1 Device structure and material characterization of the CCPS lateral memristor. (a) Schematic diagrams of the CCPS lateral memristor and its extension into a physical reservoir array through periodic repetition of unit cells. (b) Optical image of CCPS lateral memristor fabricated on a Si/SiO_2 substrate. Scale bar: 5 μm. (c) EDS elemental maps of a CCPS nanoflake for Cu, Cr, P, and S. Scale bar: 50 μm. (d) The EDS spectrum of CCPS material showing the Cu:Cr:P:S composition ratio of 1:1:2:6.

Material (ESM)). Raman spectra (Fig. S2 in the ESM) confirm structural integrity through characteristic vibrational modes at 202, 263, 378, and 589 cm^{-1}, consistent with prior reports [26, 27].

Tunable ionic conduction was characterized through consecutive I–V sweeps. The current rises rapidly at low bias (V < 2 V) and gradually saturates above 2 V (Fig. 2(a)), consistent with cumulative ionic redistribution [28, 29]. The saturation current increased from 0.22 to 25.9 nA as the cycle number increased from 20 to 100. Ionic conductance modulation exhibits strong scan-rate dependence. At positive bias (0–10 V), reducing the scan rate from 0.3 to 0.03 V/s increased the saturation current from 0.46 to 5.3 nA (Fig. 2(b)), confirming slower scans promote complete Cu^+ ion redistribution [30]. Analogous behavior was also obtained under negative bias (0 to −10 V) (Fig. 2(c)), with the saturation current evolving from −4.3 to −51.1 pA, demonstrating bidirectional ionic conduction governed by the polarity of the applied field (Fig. 2(d)). The cycle-dependent current increase, scan-rate dependence, and polarity-dependent response consistently indicate an electric-field-driven redistribution of mobile Cu^+ ions. These observations suggest that the device conductance is governed by ion accumulation and relaxation.

Current–time (I–t) measurements further support field-activated ionic transport in layered CCPS. Below the threshold bias of 0.8 V, near-constant current indicates electronic conduction dominance (Fig. 2(f)) [31, 32]. Above the threshold bias (V > 0.8 V), the monotonic current ascent signifies Cu^+ ion migration and migration between vacancies. This two-stage temporal evolution originates from anisotropic Cu^+ ion transport in layered CCPS. Cu^+ ion migration is expected to be faster within the vdW layers than across the interlayer direction, where longer hopping distances and a higher effective barrier slow redistribution. Consistently, an activation energy of ~ 0.72 eV is extracted for ionic relaxation, suggesting that thermally activated, barrier-limited transport governs the late-time dynamics [18, 33, 34]. Accordingly, the I–V hysteresis can be described by a four-stage process (Fig. 2(e)). During the forward sweep (0 to +10 V), Cu^+ ion migrates from the anode toward the cathode and accumulates near the cathode, switching the device from the high-resistance state (HRS, state I) to the low-resistance state (LRS, state II). Upon reversing the bias, back-migration drives the device toward HRS (state II to state III), followed by a transition back to LRS under continued bias (state III to state IV). At higher voltages, additional Cu^+ ion accumulation

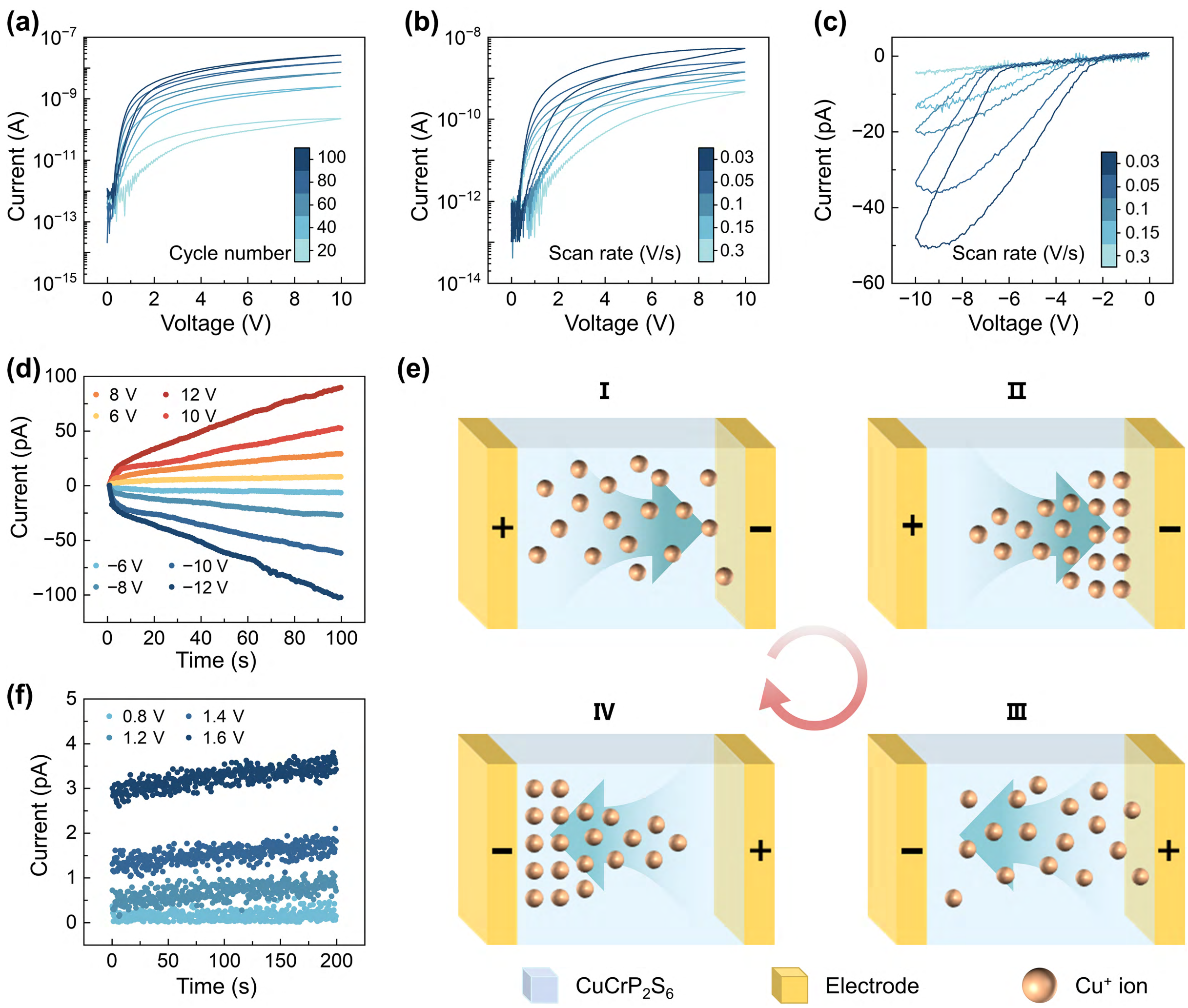

Figure 2 Electrical characteristics and field-driven ionic conductivity regulation of the CCPS lateral memristor. (a) I–V characteristics measured over 100 consecutive voltage-sweep cycles. (b) I–V curves measured under positive bias at different scan rates. (c) I–V curves measured under negative bias at different scan rates. (d) I–t responses of the device under constant bias voltages of ±6, ±8, ±10, and ±12 V. (e) Schematic illustration of the proposed four-stage Cu^+ ion redistribution process during resistive-state evolution under an external electric field. (f) I–t characteristics measured under different low positive constant bias voltages.

near the electrode may form an asymmetric interfacial barrier, contributing to the nonlinear conductance evolution [35, 36]. Thus, these results establish electric-field-tunable ionic conduction in CCPS, providing intrinsic nonlinearity and temporal dynamics for subsequent synaptic and RC functions [10, 12].

2.2 Synaptic plasticity and temporal dynamics

Electric-field-driven Cu^{+} ion migration and relaxation impart continuously tunable, history-dependent conductance, enabling synaptic plasticity in CCPS device [9, 37, 38]. Because conductance modulation is governed by ionic dynamics, it can be programmed by pulse amplitude, pulse duration, and pulse number. Single-pulse measurements show that when the pulse duration is fixed at 10 s, the minimum postsynaptic current immediately following this maximum peak ($I_{p,min}$) rises from 18.6 to 171.2 pA as the pulse amplitude (V_p) increases from 22 to 30 V (Fig. 3(a)). As the pulse duration is extended from 5 to 15 s (with a fixed pulse amplitude of 20 V), the $I_{p,min}$ increases from 31.9 to 134.8 pA (Fig. 3(b)). Paired-pulse facilitation (PPF) further captures the intrinsic temporal dynamics of the device. The decay of PPF with increasing inter-pulse interval follows a double-exponential relationship: $\mathrm{PPF}(\Delta t) = C_0 + C_1 e^{(-\Delta t/\tau_1)} + C_2 e^{(-\Delta t/\tau_2)}$. As shown in Fig. 3(c), the PPF index reaches a maximum of 275% at an inter-pulse interval of 0.2 s and decays with increasing interval following a double-exponential behavior, yielding characteristic relaxation times of τ_1 = 0.25 s and τ_2 = 5.27 s. This behavior indicates that the device state is not determined solely by the instantaneous input, but also retains a decaying trace of recent stimulation history. Such history-

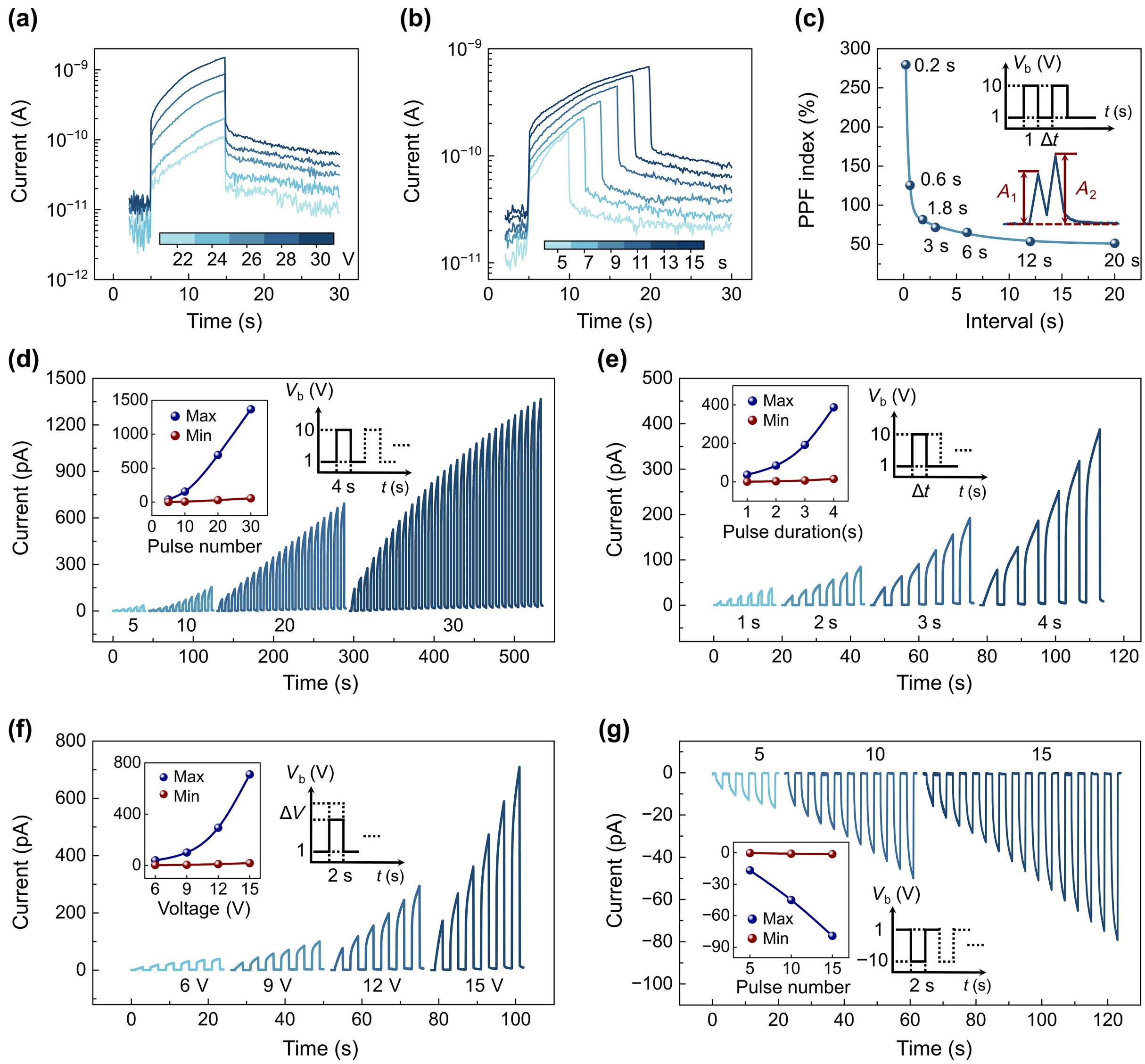

Figure 3 Synaptic plasticity of CCPS lateral memristor. (a) *I*–*t* responses to single programming pulses with amplitudes of 22–30 V at a fixed pulse width of 10 s. (b) *I*–*t* responses to single programming pulses with pulse widths of 5–15 s at a fixed pulse amplitude of 20 V. (c) PPF index plotted against inter-pulse interval (0.2–20 s). The PPF index is defined as A_2/A_1, where A_1 represents the peak current after the first pulse, and A_2 represents the peak current after the second pulse. Inset: Paired-pulse programming scheme (pulse duration: 1 s, pulse amplitude: 10 V, read voltage: 1 V) and the corresponding *I*–*t* responses at an interval of 0.2 s. (d) *I*–*t* responses under programming pulses with different pulse numbers. Inset: Plot of the extracted $I_{p,max}$ and $I_{p,min}$ versus pulse number. (e) *I*–*t* responses under programming pulses with different pulse durations. Inset: Plot of the extracted $I_{p,max}$ and $I_{p,min}$ versus pulse duration. (f) *I*–*t* responses under programming pulses with different pulse amplitudes. Inset: Plot of the extracted $I_{p,max}$ and $I_{p,min}$ versus pulse amplitude. (g) *I*–*t* responses under repeated negative programming pulses with different pulse numbers. Inset: Plot of the extracted $I_{p,max}$ and $I_{p,min}$ versus pulse number.

Tsinghua University Press | SciOpen

dependent relaxation defines a finite short-term memory window, allowing successive inputs to be temporally integrated rather than processed independently. Therefore, the PPF dynamics provide direct physical evidence that the CCPS device satisfies the fading-memory requirement of reservoir computing.

Figures 3(d)–3(g) summarize the conductance modulation of the CCPS lateral memristor under pulse programming with different pulse numbers, durations, and amplitudes. When 10 V programming pulses with a duration of 4 s were applied and a 1 V read bias was used after each pulse train, increasing the pulse number from 5 to 30 caused the maximum peak current ($I_{p,max}$) to rise from 36.8 to 1367.3 pA, while $I_{p,min}$ increased from 0.82 to 55.7 pA (Fig. 3(d)). When the pulse number was fixed at five and the pulse amplitude was kept constant, extending the pulse duration from 1 to 4 s increased the $I_{p,max}$ from 37.1 to 387.6 pA and $I_{p,min}$ from 0.93 to 15.5 pA (Fig. 3(e)). Likewise, when the pulse number and duration were fixed, increasing the pulse amplitude from 6 to 15 V led to a corresponding increase in $I_{p,max}$ from 39.8 to 709.7 pA and in $I_{p,min}$ from 2.6 to 18.1 pA (Fig. 3(f)). The insets of Figs. 3(d)–3(f) summarize the extracted $I_{p,max}$ and $I_{p,min}$ at each stimulation stage. Both metrics exhibit consistent trends, indicating cumulative ionic redistribution under stronger or more sustained stimulation. By contrast, when −10 V programming pulses with a duration of 2 s were applied, increasing the pulse number from 5 to 15 shifted the device response in the opposite direction: The $I_{p,max}$ changed from −16.7 to −79.3 pA, while $I_{p,min}$ decreased from −0.22 to −1.34 pA (Fig. 3(g)). Taken together, these pulse responses demonstrate analog, bidirectional weight updates with multi-timescale relaxation, which are essential for nonlinear processing with fading memory. Importantly, the output current does not scale linearly with pulse amplitude, duration, or pulse number; instead, it evolves in a history-dependent and progressively saturating manner, indicating nonlinear input-state mapping. Such nonlinear transformation is a key requirement for reservoir computing, because it enables the device to project temporally correlated inputs into a richer state space [39, 40].

2.3 Reservoir computing with CCPS lateral memristor

Figure 4(a) shows a CCPS lateral memristor-based RC scheme, in which inputs were encoded into temporal pulse trains and injected into a dynamic reservoir, while only the linear readout was trained [1, 2]. Specifically, the input data were first converted into voltage

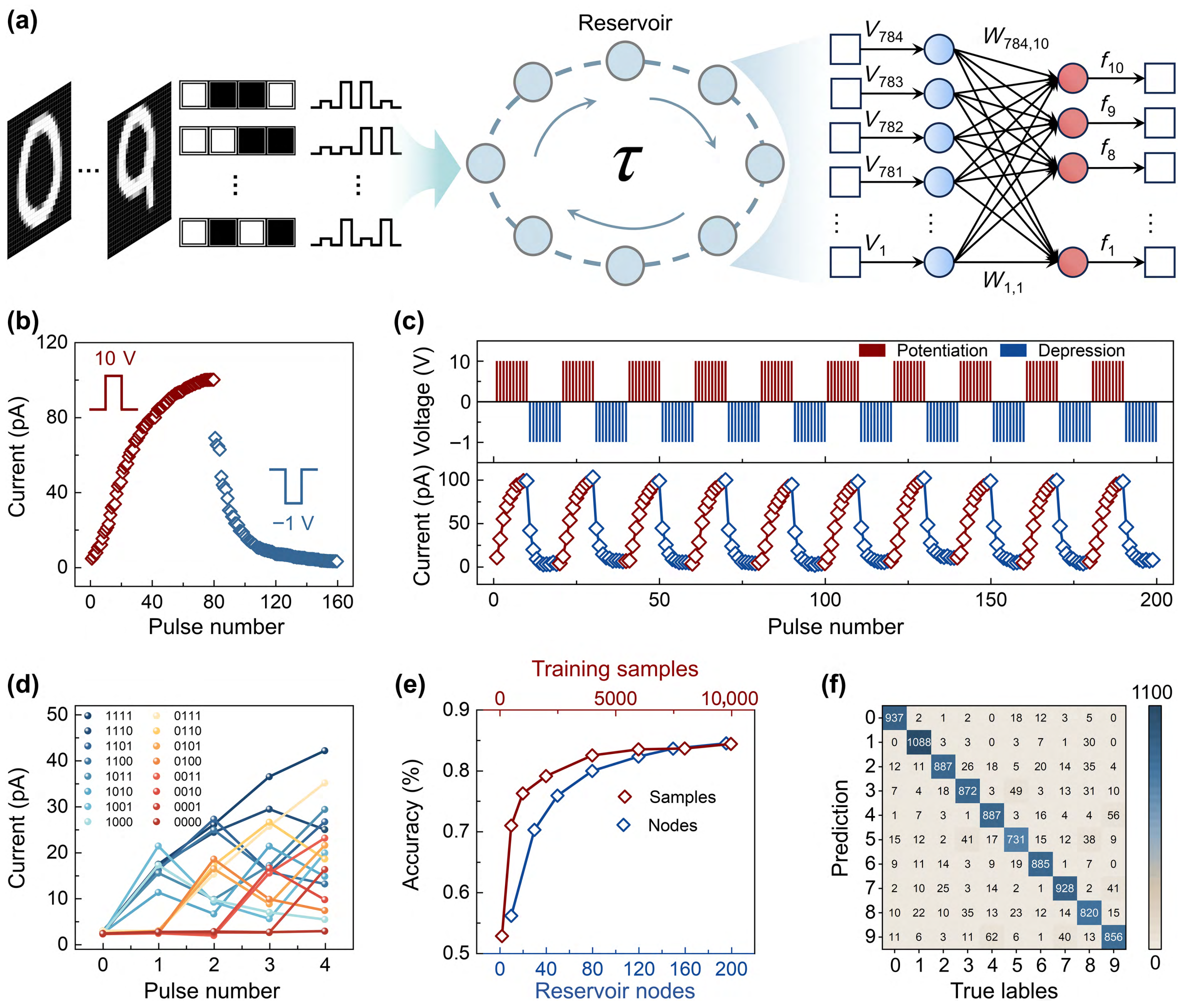

Figure 4 Reservoir computing using a CCPS lateral memristor. (a) Schematic of the time-multiplexed RC framework. Inputs were encoded into temporal pulse trains and injected into a CCPS lateral memristor as a physical reservoir, while only the linear readout was trained. (b) Potentiation–depression current curves measured under positive and negative programming pulses of 10 and −1 V. (c) Cycling test of the potentiation–depression behavior (set/reset voltages: 10 V/−1 V; read voltage: 2 V). (d) Summary of the device responses to the encoded input pulse trains. (e) Recognition accuracy versus training-sample size and reservoir-node number. (f) Confusion matrix for MNIST classification obtained from the CCPS-based physical reservoir computing system.

pulse trains that could be directly applied to the device. Under these temporally encoded inputs, the conductance of the CCPS lateral memristor evolved in a history-dependent manner, thereby generating reservoir states through its intrinsic nonlinear and fading-memory dynamics. The resulting state vectors were then collected and fed into a linear readout layer, while the reservoir itself remained fixed during training [10, 41]. To assess the device as a physical reservoir, pulse-programmable analog conductance updates were first verified. Monotonic potentiation and depression with multilevel states were obtained using 10 and −1 V programming pulses, followed by a 2 V read pulse voltage after each programming pulse (Fig. 4(b)), enabling bidirectional and continuous conductance modulation. The extracted nonlinearity factors (NLF) were 2.45 for LTP and 5.31 for LTD, indicating moderately asymmetric but analog weight updates [42, 43]. Reproducibility was further confirmed over ten successive potentiation–depression cycles, during which the intermediate conductance states remained uniform and well separated (Fig. 4(c)). The distributions of these intermediate conductance states remained concentrated, with limited fluctuation and no obvious degradation in the switching window. In addition, cycle-by-cycle fitting of the potentiation branch showed that the extracted nonlinearity factors remained close to 2, while the fitted G_{min}, NL, and MSE exhibited only limited variation across the ten cycles (Fig. S4 in the ESM), further confirming stable and reproducible analog weight updating behavior under repeated operation. To benchmark learning enabled by the device-level plasticity, a convolutional neural network (CNN) was constructed using the measured LTP/LTD characteristics and evaluated on the MNIST handwritten digit dataset, achieving an accuracy of 96.49% (Fig. S5 in the ESM) [44].

The CCPS lateral memristor was further employed as a physical reservoir for image recognition tasks within an in-materia computing paradigm [11, 45]. By encoding input information into temporal pulse trains and directly injecting them into the device, stable and well-resolved multilevel current responses were obtained (Fig. 4(d)). In this framework, temporal encoding defines how the original data are mapped onto the device stimulus, whereas the subsequent conductance evolution determines the reservoir-state representation used for classification (Fig. S6 in the ESM). The RC system constructed from this physical reservoir achieved a recognition accuracy of 88.91% on the MNIST test set, closely matching the training accuracy (88.61%), indicating effective suppression of overfitting (Table S1 in the ESM). Increasing either the number of reservoir nodes or the size of the training set led to a gradual improvement in classification accuracy. Specifically, when the training set was fixed at 10,000 samples, the accuracy increased with reservoir node number and reached 84.5% at 196 nodes. Conversely, when the number of reservoir nodes was fixed at 196, the accuracy increased with training set size and reached 84.4% at 10,000 samples. Further increasing the training set to the full 60,000 MNIST samples produced the final test accuracy of 88.91% (Fig. 4(e) and Fig. S8 in the ESM). Although this accuracy was modest compared with large-scale digital neural networks, it was achieved within an in-materia computing paradigm, where computation was performed directly through the material's intrinsic ionic transport, nonlinear conductance modulation, and relaxation dynamics rather than through software-based floating-point operations. In this framework, nonlinear mapping and temporal memory emerged naturally from the physical response of the CCPS device, highlighting a fundamentally different trade-off between numerical precision and physical efficiency. Besides, benefiting from the non-iterative training scheme of reservoir computing and the analog, passive nature of the memristive reservoir, training on the full MNIST dataset (60,000 samples) was completed within 63.1 s, representing a substantial reduction in computational overhead compared with conventional GPU-based convolutional neural networks [14]. The confusion matrix was dominated by diagonal entries (Fig. 4(f)), indicating low misclassification and near-linear separability in the reservoir state space.

To evaluate the capability of the CCPS-based physical reservoir for temporal information processing, waveform classification was first performed as a preliminary benchmark (Fig. 5(a)). Under optimized conditions, a test accuracy of 99.5% was achieved. The classification accuracy increased with the number of virtual nodes, confirming that the CCPS-based physical reservoir effectively expanded the input into a high-dimensional state space through time multiplexing.

The system was further assessed using chaotic time-series prediction, which represented a more stringent test of dynamical modeling capability. Chaotic systems were highly sensitive to initial conditions, such that small prediction errors could rapidly accumulate and lead to trajectory divergence [31]. This property made chaotic benchmarks well suited for evaluating whether reservoir computing systems captured complex nonlinear dynamics. The Hénon map and the Mackey-Glass time series were therefore adopted as representative cases, spanning discrete strongly chaotic dynamics with rapid error growth and continuous delay-induced chaos with extended short-term predictability.

The Hénon map is described by the following discrete iterative equations: $x(n+1)=y(n)-ax(n)^2$ and $y(n+1)=bx(n)$. Using parameters a = 1.4 and b = 0.3, a time series of length 1000 is generated via numerical iteration. The first 500 time steps were used for training, after which the external input was removed and autonomous prediction was initiated. As shown in Fig. 5(b), the system yielded a normalized root-mean-square error (NRMSE) of 0.02732 and a coefficient of determination (R^2) of 0.992 during the early stage of autonomous prediction (steps 500–550). With increasing prediction horizon, however, accumulated errors lead to noticeable divergence beyond approximately 550 time steps, which is characteristic of long-term prediction in strongly chaotic systems (Fig. 5(c)) [32].

Importantly, even after divergence occurs, the generated sequence does not collapse into random noise but instead preserves dynamical features similar to those of the target Hénon map, including comparable amplitude distributions and oscillatory structure. Such phase drift is unavoidable in long-horizon chaotic prediction, yet the ability of the system to reproduce the overall geometry of the chaotic attractor indicates that the underlying dynamics of the target system are successfully captured. Consistently, when the mask is removed or the effective reservoir dimension is significantly reduced, the predicted sequence rapidly decays and loses its chaotic characteristics (Fig. S7 in the ESM), highlighting the necessity of high-dimensional state expansion for chaotic modeling.

Prediction was further evaluated on the Mackey-Glass time series using the same training-autonomous protocol under two representative delay settings, τ = 17 (near the onset of chaos) and τ = 30 (deeper in the chaotic regime). The Mackey-Glass dynamics are governed by the following delay differential equation:

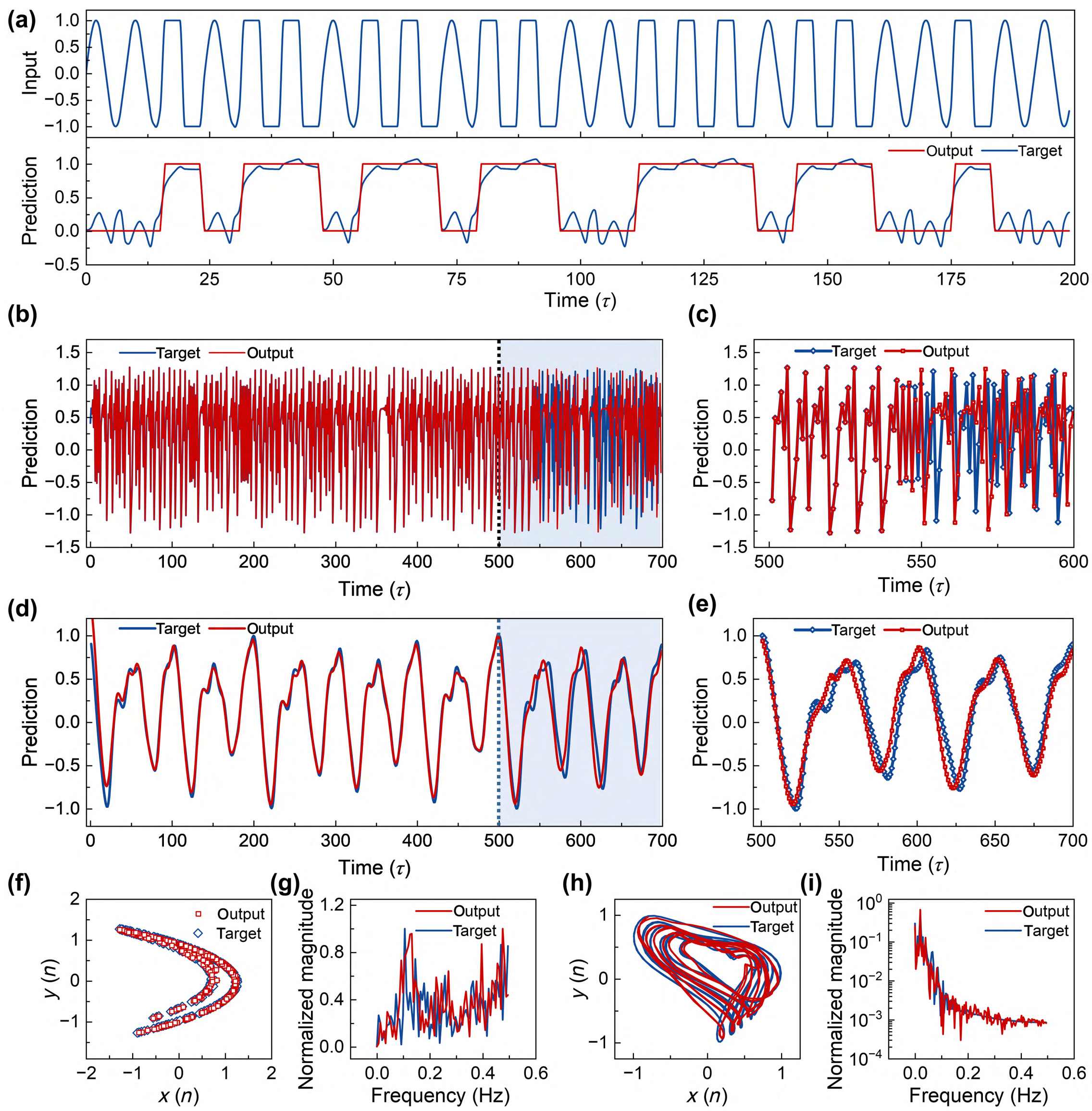

Figure 5 Chaotic time-series prediction with the CCPS-based physical reservoir. (a) Waveform classification with a physical reservoir. (b) Hénon map time-series prediction result, where the blue curve denotes the ideal target and the red curve represents the experimental output of the RC system (M = 4, N = 25, V_{max} = 3.0 V). (c) Enlarged view of the autonomous prediction window for the Hénon map (500–600 time steps). (d) Mackey-Glass prediction result, with the experimental parameters the same as those used for the Hénon map task. (e) Enlarged view of the autonomous prediction window for the Mackey-Glass series (500–700 time steps). Phase-space reconstruction (f) and corresponding frequency-domain spectrum (g) for the Hénon map prediction. Phase-space reconstruction (h) and corresponding frequency-domain spectrum (i) for the Mackey-Glass prediction.

$\frac{\mathrm{d}x}{\mathrm{d}t}=\beta\frac{x(t-\tau)}{1+x^{n}(t-\tau)}-\gamma x(t)$. Chaotic behavior emerges when the delay parameter exceeds $\tau > 16.8$. Under both delay conditions, stable autonomous prediction was maintained over the 500–700 time-step interval (Figs. 5(d) and 5(e)), showing improved long-term agreement relative to the Hénon map case. In particular, within the early autonomous window (500–600 steps), the prediction error reached NRMSE = 0.3716. Consistent overlap between the predicted and target trajectories was further confirmed in phase space (Figs. 5(f) and 5(h)) and in the frequency domain (Figs. 5(g) and 5(i)) [30, 37]. Together, these results consistently demonstrate that the CCPS-based physical reservoir effectively captured the essential dynamical features of both chaotic systems across time, phase space, and frequency domains. Overall, the proposed CCPS-RC system exhibited robust performance in chaotic time-series prediction, highlighting its ability to exploit intrinsic ionic dynamics for parallel computation and temporal information processing.

3 Conclusion

In this study, a two-terminal CCPS lateral memristor was fabricated and demonstrated as a physical reservoir computing. The device exhibited I–V hysteresis and electric-field-tunable ionic conduction, consistent with reversible Cu^{+} ion redistribution and interfacial accumulation, which together provide an intrinsic source of nonlinearity and relaxation dynamics. Under pulse programming, synaptic plasticity was achieved through analog, bidirectional conductance updates, and paired-pulse facilitation further revealed multi-timescale relaxation that supports fading memory for temporal processing. Building on these device-level properties, a single CCPS lateral memristor was implemented as a physical reservoir within an in-materia computing paradigm, where nonlinear mapping and memory arise directly from the material response rather than from explicit numerical operations. With time-multiplexed encoding, well-resolved multilevel current states supported temporal processing for pattern recognition and dynamical forecasting. The resulting system achieved 88.91% accuracy on MNIST handwritten digit recognition, with training on the full 60,000 sample dataset completed in 63.1 s. Robust chaotic prediction was also demonstrated, yielding autonomous–prediction-stage NRMSE of 0.02732 for the Hénon map and 0.3716 for the Mackey-Glass time series. Overall, these results establish CCPS lateral memristors as a physically interpretable reservoir platform for temporal information processing, highlighting the potential of Cu^+ ion migration-driven device dynamics for integrating material functionality with system-level reservoir computing.

4 Experiments

4.1 Device fabrication and characterization

CCPS nanoflakes were mechanically exfoliated from bulk crystals purchased from Nanjing MKNANO Technology and then transferred onto Si/SiO_2 substrates with a 285 nm-thick oxide layer via a PDMS-assisted transfer process. The flake positions were identified using an optical microscope (Nikon LV150N). Source-drain electrode patterns were defined by electron-beam lithography (EBL), followed by thermal evaporation of Cr/Au (10/50 nm) with deposition rates of 0.1 and 0.4 Å/s for Cr and Au, respectively. Finally, a lift-off process was performed to complete the device structure.

The thickness of the CCPS nanoflakes was characterized by AFM (Asylum Research MFP-3D). Raman spectroscopy of the CCPS nanoflakes was also characterized on the device using a laser confocal Raman spectrometer (Finder 930, 532 nm excitation laser). The electrical characteristics of the CCPS device were measured using an FS-Pro semiconductor parameter analyzer.

4.2 Calculation of nonlinearity factor

The measured LTP/LTD curves were fitted with parametric models. The LTP branch used a single-exponential growth function, whereas the LTD branch used a double-exponential decay because a single-exponential fit produced nonphysical parameters. The nonlinearity metric was computed from the fitted parameters, and the fitted model was sampled to build a normalized lookup table (LUT) for training. During online learning, weights were updated using the Adam optimizer and then weakly projected onto the nearest lookup-table level with projection strength α [29]. The LTP and LTD characteristics are fitted using the following expressions: $G_{\mathrm{LTP}}(P)=B(1-\mathrm{e}^{-P/A})+G_{\min}$ and $G_{\mathrm{LTD}}(P)=-B_1(1-\mathrm{e}^{(P-P_{\max})/A_1})-B_2(1-\mathrm{e}^{(P-P_{\max})/A_2})+G_{\max}$. Here, $G_{\mathrm{LTP}}(P)$ and $G_{\mathrm{LTD}}(P)$ represent the instantaneous conductance values during the potentiation and depression processes, respectively. The parameters $G_{\max}$ and $G_{\min}$ denote the maximum and minimum conductance values extracted directly from the experimental saturation levels. P indicates the current pulse index, while $P_{\max}$ represents the total number of pulses required to switch the device between the extreme conductance states. The parameter A serves as the characteristic nonlinearity parameter, governing the curvature of the weight update trajectory. A smaller A indicates a more abrupt, highly non-linear saturation, whereas a larger A implies a more linear response. The coefficient B acts as a normalization factor, defined as $B=(G_{\max}-G_{\min})/(1-\mathrm{e}^{-P_{\max}/A})$, ensuring that the fitted curve strictly spans the range $[G_{\min}, G_{\max}]$. Based on the extracted parameter A, a standardized NL was computed using the empirical relation: $\mathrm{NL}=1.726/(A+0.162)-P_{\max}/A$. The calculated NLFs are 2.45 for LTP and 5.31 for LTD (Fig. S3 in the ESM). The fitted analytical models were subsequently sampled to construct a normalized LUT. During the offline learning phase, this LUT was utilized to map the ideal algorithmic weight updates to the realistic, non-linear conductance states of the hardware, ensuring high-fidelity simulation of the device's synaptic behavior.

4.3 Physics-driven dynamics modeling and parameter extraction

To faithfully capture the essence of in-materia computing in simulation, a phenomenological dynamics model was developed for the CCPS memristor, rather than adopting generic nonlinear activation functions. The conductance evolution was described by an internal state variable *G(t)* governed by a recursive update rule: $G_{t+1}=rG_t+(1-r)G_0+\eta(V_t)(I(V_t)-G_t)$. In this formulation, the memory retention factor $r\approx 0.9748$ sets the depth of fading memory and thus provides the physical basis for temporal dependency in the reservoir. The voltage dependent update rate $\eta(V_t)$ captures electric-field modulation of the ionic migration barrier, which introduces the required nonlinearity into the state dynamics. Model parameters were identified by global optimization using a differential evolution (DE) algorithm, where the optimal parameter set minimized the mean squared error between simulated currents and experimentally measured responses under both single-pulse and multi-pulse excitations. This procedure yielded a high-fidelity device digital twin suitable for reservoir level simulations [46].

4.4 Dual-voltage bidirectional scanning reservoir architecture

Building on the physics-driven device model described above, a spatiotemporal feature-extraction architecture was designed for static image tasks such as MNIST. Each 28 × 28 image was first reduced in dimension and then converted into a length-196 voltage pulse sequence using 4-bit LUT encoding. To mitigate the causality constraint of a single physical device in time-multiplexed processing, where the imposed pixel ordering can cause early information to fade, a dual-voltage bidirectional scanning strategy was introduced. The same input sequence was injected in both the forward and backward directions. Each direction was driven under two voltage regimes. The low-voltage setting used Scale = 0.035 and corresponded to a quasi-linear, memory-dominant regime. The high-voltage setting used Scale = 0.07 and corresponded to a nonlinear, near-saturation regime. This design leveraged voltage-dependent device dynamics. The quasi-linear regime favored longer memory retention, whereas the nonlinear regime enhanced nonlinear feature mapping. Together, these complementary responses expanded the effective state space of the physical reservoir and improved spatiotemporal representation capacity.

4.5 Readout and classification

The final feature vector was constructed by concatenating the device conductance-evolution sequences obtained under the four operating states, namely forward and backward scans combined with low and high voltage driving. This procedure produced a high-dimensional spatiotemporal representation. Such a construction effectively replaced the large random connectivity used in conventional reservoirs and relied entirely on the device's intrinsic physical properties for information processing. For classification, the concatenated high-dimensional features were fed into either a logistic regression or a ridge regression classifier. Because the reservoir layer parameters, corresponding to the physics-based model, were fixed and physically grounded, training required only fine-tuning the linear weights of the readout layer. This not only reduced the computational cost substantially but also confirmed the effectiveness of the physical reservoir architecture in generating linearly separable features.

Electronic Supplementary Material: Supplementary material (SEM image and EDS characterization of a pristine CCPS nanoflake; Raman spectrum of CCPS nanoflake; fitting of P/D characteristics; cycle-to-cycle stability analysis of the potentiation characteristics over ten successive P/D cycles; CNN baseline results for handwritten digit recognition; image-to-pulse encoding scheme for MNIST processing using a physics-driven memristive reservoir; rapid decay during autonomous prediction of the Mackey-Glass time series; comparison of representative memristor-based reservoir computing systems; optimized model parameters for reproducing experimental current dynamics; optimized configuration for autonomous Mackey–Glass prediction) is available in the online version of this article at https://doi.org/10.26599/NR.2026.94908805.

Data availability

All data needed to support the conclusions in the paper are presented in the manuscript and the Electronic Supplementary Material. Additional data related to this paper may be requested from the corresponding author upon request.

Acknowledgement

This work is supported by the National Natural Science Foundation of China (No. 52403344), the Key Research & Development Program of Guangxi (No. AB24010033), the Special Project for Guangxi Science and Technology Base and Talent (No. AD25069071), and Innovation Research Foundation of National University of Defense Technology.

Declaration of competing interest

All the contributing authors report no conflict of interests in this work.

Author contribution statement

Y. Q. H.: Conceptualization, methodology, investigation, data curation, formal analysis, writing – original draft, writing – review & editing. R. H. Z.: Investigation, validation, data curation, writing – review & editing. J. X. C.: Investigation, validation, writing – review & editing. L. Q. C.: Investigation, formal analysis. Z. H. L.: Investigation, validation. C. H.: Investigation, data curation. J. H. Y.: Investigation, validation, writing – review & editing. N. L.: Investigation, resources, writing – review & editing. B. B. Z.: Investigation, validation, writing – review & editing. Q. D.: Investigation, resources, writing – review & editing. X. C. L.: Investigation, validation. Z. R. Z.: Supervision, funding acquisition, project administration. Q. J. S.: Supervision, funding acquisition, project administration, writing – review & editing. J. R. Y.: Conceptualization, supervision, funding acquisition, project administration, writing – review & editing. C. F. Z.: Supervision, funding acquisition, project administration, writing – review & editing. All the authors have approved the final manuscript.

Use of AI statement

None.

References

[1] Lukoševičius, M.; Jaeger, H. Reservoir computing approaches to recurrent neural network training. *Comput. Sci. Rev.* **2009**, *3*, 127–149.
[2] Verstraeten, D.; Schrauwen, B.; D'Haene, M.; Stroobandt, D. An experimental unification of reservoir computing methods. *Neural Netw.* **2007**, *20*, 391–403.
[3] Maass, W.; Natschläger, T.; Markram, H. Real-time computing without stable states: A new framework for neural computation based on perturbations. *Neural Comput.* **2002**, *14*, 2531–2560.
[4] Elman, J. L. Finding structure in time. *Cogn. Sci.* **1990**, *14*, 179–211.
[5] Nakajima, K. Physical reservoir computing-an introductory perspective. *Jpn. J. Appl. Phys.* **2020**, *59*, 060501.
[6] Qi, Z. Y.; Mi, L. J.; Qian, H. R.; Zheng, W. G.; Guo, Y.; Chai, Y. Physical reservoir computing based on nanoscale materials and devices. *Adv. Funct. Mater.* **2023**, *33*, 2306149.
[7] Du, C.; Cai, F. X.; Zidan, M. A.; Ma, W.; Lee, S. H.; Lu, W. D. Reservoir computing using dynamic memristors for temporal information processing. *Nat. Commun.* **2017**, *8*, 2204.
[8] Midya, R.; Wang, Z. R.; Asapu, S.; Zhang, X. M.; Rao, M. Y.; Song, W. H.; Zhuo, Y.; Upadhyay, N.; Xia, Q. F.; Yang, J. J. Reservoir computing using diffusive memristors. *Adv. Intell. Syst.* **2019**, *1*, 1900084.
[9] Moon, J.; Ma, W.; Shin, J. H.; Cai, F. X.; Du, C.; Lee, S. H.; Lu, W. D. Temporal data classification and forecasting using a memristor-based reservoir computing system. *Nat. Electron.* **2019**, *2*, 480–487.
[10] Sun, L. F.; Wang, Z. R.; Jiang, J. B.; Kim, Y.; Joo, B.; Zheng, S. J.; Lee, S.; Yu, W. J.; Kong, B. S.; Yang, H. In-sensor reservoir computing for language learning via two-dimensional memristors. *Sci. Adv.* **2021**, *7*, eabg1455.
[11] Milano, G.; Pedretti, G.; Montano, K.; Ricci, S.; Hashemkhani, S.; Boarino, L.; Ielmini, D.; Ricciardi, C. *In materia* reservoir computing with a fully memristive architecture based on self-organizing nanowire networks. *Nat. Mater.* **2022**, *21*, 195–202.
[12] Zhong, Y. N.; Tang, J. S.; Li, X. Y.; Gao, B.; Qian, H.; Wu, H. Q. Dynamic memristor-based reservoir computing for high-efficiency temporal signal processing. *Nat. Commun.* **2021**, *12*, 408.
[13] Zhang, J. H.; Zhu, Z. Q.; Meng, J. L.; Wang, T. Y. Fiber memristor-based physical reservoir computing for multimodal sleep monitoring. *Research* **2025**, *8*, 0870.
[14] Zhong, Y. N.; Tang, J. S.; Li, X. Y.; Liang, X. P.; Liu, Z. W.; Li, Y. J.; Xi, Y.; Yao, P.; Hao, Z. Q.; Gao, B. et al. A memristor-based analogue reservoir computing system for real-time and power-efficient signal processing. *Nat. Electron.* **2022**, *5*, 672–681.
[15] Jiang, X. G.; Wang, X. Y.; Wang, X. L.; Zhang, X. P.; Niu, R. R.; Deng, J. M.; Xu, S.; Lun, Y.; Liu, Y. Y.; Xia, T. L. et al. Manipulation of current rectification in van der Waals ferroionic $CuInP_2S_6$. *Nat. Commun.* **2022**, *13*, 574.

[16] Wu, Y. W.; Duong, N. T.; Chien, Y. C.; Liu, S.; Ang, K. W. A dynamic memory for reservoir computing utilizing ion migration in $CuInP_2S_6$. *Adv. Electron. Mater.* **2024**, *10*, 2300481.

[17] Liu, Y. Q.; Wu, Y. H.; Han, H. J.; Wang, Y.; Peng, R. X.; Liu, K.; Yi, D.; Nan, C. W.; Ma, J. $CuInP_2S_6$-based electronic/optoelectronic synapse for artificial visual system application. *Adv. Funct. Mater.* **2024**, *34*, 2306945.

[18] Cheng, X.; Zhong, Z. P.; Zhuang, Y. Z.; Wang, W.; Yang, Q. Y.; Li, X.; Shi, W.; Meng, X. J.; Cao, Y. N.; Wang, J. L. et al. High precision conductance modulation in $CuCrP_2S_6$ synaptic devices for enhanced neuromorphic computing. *Adv. Funct. Mater.* **2025**, *35*, 2504017.

[19] Yang, Y. C.; Huang, R. Probing memristive switching in nanoionic devices. *Nat. Electron.* **2018**, *1*, 274–287.

[20] Wang, T. Y.; Meng, J. L.; Rao, M. Y.; He, Z. Y.; Chen, L.; Zhu, H.; Sun, Q. Q.; Ding, S. J.; Bao, W. Z.; Zhou, P. et al. Three-dimensional nanoscale flexible memristor networks with ultralow power for information transmission and processing application. *Nano Lett.* **2020**, *20*, 4111–4120.

[21] Wang, T. Y.; Meng, J. L.; Zhou, X. F.; Liu, Y.; He, Z. Y.; Han, Q.; Li, Q. X.; Yu, J. J.; Li, Z. H.; Liu, Y. K. et al. Reconfigurable neuromorphic memristor network for ultralow-power smart textile electronics. *Nat. Commun.* **2022**, *13*, 7432.

[22] Choi, S.; Yang, J.; Wang, G. Emerging memristive artificial synapses and neurons for energy-efficient neuromorphic computing. *Adv. Mater.* **2020**, *32*, 2004659.

[23] Jeon, K.; Kim, J.; Ryu, J. J.; Yoo, S. J.; Song, C.; Yang, M. K.; Jeong, D. S.; Kim, G. H. Self-rectifying resistive memory in passive crossbar arrays. *Nat. Commun.* **2021**, *12*, 2968.

[24] Wu, C. X.; Kim, T. W.; Choi, H. Y.; Strukov, D. B.; Yang, J. J. Flexible three-dimensional artificial synapse networks with correlated learning and trainable memory capability. *Nat. Commun.* **2017**, *8*, 752.

[25] Maisonneuve, V.; Cajipe, V. B.; Payen, C. Low-temperature neutron powder diffraction study of copper chromium thiophosphate ($CuCrP_2S_6$): Observation of an ordered, antipolar copper sublattice. *Chem. Mater.* **1993**, *5*, 758–760.

[26] Susner, M. A.; Rao, R.; Pelton, A. T.; McLeod, M. V.; Maruyama, B. Temperature-dependent Raman scattering and X-ray diffraction study of phase transitions in layered multiferroic $CuCrP_2S_6$. *Phys. Rev. Mater.* **2020**, *4*, 104003.

[27] Ma, Y. C.; Yan, Y.; Luo, L. Q.; Pazos, S.; Zhang, C. H.; Lv, X.; Chen, M. L.; Liu, C.; Wang, Y. Z.; Chen, A. T. et al. High-performance van der Waals antiferroelectric $CuCrP_2S_6$-based memristors. *Nat. Commun.* **2023**, *14*, 7891.

[28] Vandoorne, K.; Mechet, P.; Van Vaerenbergh, T.; Fiers, M.; Morthier, G.; Verstraeten, D.; Schrauwen, B.; Dambre, J.; Bienstman, P. Experimental demonstration of reservoir computing on a silicon photonics chip. *Nat. Commun.* **2014**, *5*, 3541.

[29] Duport, F.; Smerieri, A.; Akrout, A.; Haelterman, M.; Massar, S. Fully analogue photonic reservoir computer. *Sci. Rep.* **2016**, *6*, 22381.

[30] Katumba, A.; Heyvaert, J.; Schneider, B.; Uvin, S.; Dambre, J.; Bienstman, P. Low-loss photonic reservoir computing with multimode photonic integrated circuits. *Sci. Rep.* **2018**, *8*, 2653.

[31] Taniguchi, T.; Ogihara, A.; Utsumi, Y.; Tsunegi, S. Spintronic reservoir computing without driving current or magnetic field. *Sci. Rep.* **2022**, *12*, 10627.

[32] Wang, X. Z.; Cichos, F. Harnessing synthetic active particles for physical reservoir computing. *Nat. Commun.* **2024**, *15*, 774.

[33] Wang, X. L.; Shang, Z. X.; Zhang, C.; Kang, J. Q.; Liu, T.; Wang, X. Y.; Chen, S. L.; Liu, H. L.; Tang, W.; Zeng, Y. J. et al. Electrical and magnetic anisotropies in van der Waals multiferroic $CuCrP_2S_6$. *Nat. Commun.* **2023**, *14*, 840.

[34] Ma, R. R.; Xu, D. D.; Zhong, Q. L.; Zhong, C. R.; Huang, R.; Xiang, P. H.; Zhong, N.; Duan, C. G. Nanoscale mapping of Cu-ion transport in van der Waals layered $CuCrP_2S_6$. *Adv. Mater. Interfaces* **2022**, *9*, 2101769.

[35] Yao, X. H.; Klyukin, K.; Lu, W. J.; Onen, M.; Ryu, S.; Kim, D.; Emond, N.; Waluyo, I.; Hunt, A.; Del Alamo, J. A. et al. Protonic solid-state electrochemical synapse for physical neural networks. *Nat. Commun.* **2020**, *11*, 3134.

[36] Liu, K. Q.; Dang, B. J.; Zhang, T.; Yang, Z.; Bao, L.; Xu, L. Y.; Cheng, C. D.; Huang, R.; Yang, Y. C. Multilayer reservoir computing based on ferroelectric α-In_2Se_3 for hierarchical information processing. *Adv. Mater.* **2022**, *34*, 2108826.

[37] Chen, Z. W.; Li, W. J.; Fan, Z.; Dong, S.; Chen, Y. H.; Qin, M. H.; Zeng, M.; Lu, X. B.; Zhou, G. F.; Gao, X. S. et al. All-ferroelectric implementation of reservoir computing. *Nat. Commun.* **2023**, *14*, 3585.

[38] Cheong, W. H.; Jeon, J. B.; In, J. H.; Kim, G.; Song, H. C.; An, J.; Park, J.; Kim, Y. S.; Hwang, C. S.; Kim, K. M. Demonstration of neuromodulation-inspired stashing system for energy-efficient learning of spiking neural network using a self-rectifying memristor array. *Adv. Funct. Mater.* **2022**, *32*, 2200337.

[39] Wang, W.; Wang, R.; Shi, T.; Wei, J. S.; Cao, R. R.; Zhao, X. L.; Wu, Z. H.; Zhang, X. M.; Lu, J.; Xu, H. et al. A self-rectification and quasi-linear analogue memristor for artificial neural networks. *IEEE Electron Device Lett.* **2019**, *40*, 1407–1410.

[40] Kim, Y.; Kim, J.; Kim, S. S.; Kwon, Y. J.; Kim, G. S.; Jeon, J. W.; Kwon, D. E.; Yoon, J. H.; Hwang, C. S. Kernel application of the stacked crossbar array composed of self-rectifying resistive switching memory for convolutional neural networks. *Adv. Intell. Syst.* **2020**, *2*, 1900116.

[41] Wu, C. J.; Li, X. L.; Xu, X. H.; Lee, B. W.; Chae, S. C.; Liu, C. L. Self-rectifying resistance switching memory based on a dynamic p-n junction. *Nanotechnology* **2021**, *32*, 085203.

[42] Choi, S.; Kim, Y.; Van Nguyen, T.; Jeong, W. H.; Min, K. S.; Choi, B. J. Low-power self-rectifying memristive artificial neural network for near internet-of-things sensor computing. *Adv. Electron. Mater.* **2021**, *7*, 2100050.

[43] Biju, K. P.; Liu, X. J.; Kim, S.; Siddik, M.; Shin, J.; Lee, J.; Hwang, H. Bipolar resistance switching in the Pt/WO_x/W nonvolatile memory devices. *Curr. Appl. Phys.* **2011**, *11*, e62–e65.

[44] Yu, S. M.; Guan, X. M.; Wong, H. S. P. On the switching parameter variation of metal oxide RRAM-part II: Model corroboration and device design strategy. *IEEE Trans. Electron Devices* **2012**, *59*, 1183–1188.

[45] Fang, R. R.; Zhang, W. Y.; Ren, K.; Zhang, P. W.; Xu, X. X.; Wang, Z. R.; Shang, D. S. In-materio reservoir computing based on nanowire networks: Fundamental, progress, and perspective. *Mater. Futures* **2023**, *2*, 022701.

[46] Storn, R.; Price, K. Differential evolution-a simple and efficient heuristic for global optimization over continuous spaces. *J. Glob. Optim.* **1997**, *11*, 341–359.